Infrared and Millimetric Study of the Young Outflow Cepheus E

Amaya Moro-Martín

Steward Observatory, University of Arizona, Tucson, AZ, 85721

Electronic mail: amaya@as.arizona.edu

Alberto Noriega-Crespo

SIRTF Science Center, California Institute of Technology

IPAC 100-22, Pasadena, California, 91125

Electronic mail: alberto@ipac.caltech.edu

Sergio Molinari

Infrared Processing and Analysis Center,

California Institute of Technology

Pasadena, California, 91125

Electronic mail: molinari@ipac.caltech.edu

Leonardo Testi

Osservatorio Astrofisico di Arcetri

50125 Firenze, Italy

Electronic mail: lt@arcetri.astro.it

José Cernicharo

Instituto de Estructura de la Materia

CSIC, Calle Serrano 40, Madrid, Spain

Electronic mail: cerni@astro.iem.csic

Anneila Sargent

Division of Physics, Mathematics and Astronomy

California Institute of Technology

Pasadena, California, 91125

Electronic mail: afs@astro.caltech.edu

Received;	accepted
-----------	----------

ABSTRACT

The Cepheus E outflow has been studied in the mid and far infrared using the ISO CAM and LWS instruments, and at millimetric wavelengths using OVRO. In the near and mid-IR, its morphology is similar to that expected for a jet driven outflow, where the leading bow shocks entrain and accelerate the surrounding molecular gas. As expected, fine structure atomic/ionic emission lines arise from the bow shocks, at both the Mach Disk and the stagnation tip, where J-shocks are dominant. The H₂, H₂O and CO molecular emission could arise further 'downstream' at the bow shock wings where the shocks ($v = 8 - 35 \text{ km s}^{-1}$) are oblique and more likely to be C-type. The ¹³CO emission arises from entrained molecular gas and a compact high velocity emission is observed, together with an extended low velocity component that almost coincides spatially with the H₂ near-IR emission. The millimetric continuum emission shows two sources. We identify one of them with IRAS 23011+6126, postulating is the driver of the Cepheus E outflow; the other, also an embedded source, is likely to be driving one of other outflows observed in the region. Finally, we suggest that the strong [C II] 158 μ m emission must originate from an extended photo-dissociation region, very likely excited by the nearby Cepheus OB3 association.

Subject headings: stars: formation — stars: pre-main-sequence — ISM: jets and outflows — infrared: ISM: lines and bands

1. Introduction

Low mass proto-stars produce outflows that interact mostly through shocks with the surrounding medium (e. g. Reipurth & Raga 1999). Nevertheless, the details of the earliest evolutionary steps remain somewhat unclear. The embedded flow at Cepheus E (hereafter Cep E) displays all the characteristics of an extremely young object still surrounded by a thick cocoon of cold gas (e. g. Cernicharo et al. 2000), and hence provides an ideal opportunity to study the development of molecular/ionic outflows and their surrounding environments during the earliest stages of star formation.

Cep E was identified originally as a cloud core in molecular CO observations (Sargent 1977), and subsequently, an associated outflow was discovered (see Fukui 1989; Hodapp 1994). The region around Cep E has proved more complicated than the early CO and the K' observations indicated; there are at least two other outflows besides the original compact 'North-South' H_2 flow identified by Ladd & Hodapp (1997). One is nearly perpendicular to the main H_2 flow and appears as a faint chain of H_2 1-0 S(1) 2.121 μ m emission knots towards the West (Eislöffel et al. 1996); the other is seen in the CO J = 1-0 line, is extended by $\sim 90''$ along a PA $\sim -45^{\circ}$ (Ladd & Howe 1997). All three flows arise within a 5" region around IRAS 23011+6126, which presumably encompasses the driving source (Lefloch, Eislöffel & Lazareff 1996; Noriega-Crespo, Garnavich & Molinari 1998, hereafter NCGM; Cernicharo et al. 2000). For a low mass object IRAS 23011+6126 is estimated to have a very high bolometric luminosity, $\sim 70~L_{\odot}$ (Lefloch et al. 1996), suggesting that we are dealing with a relatively massive protostar, or with a low-mass protostar in an unusually early evolutionary phase and considerable higher accretion luminosity.

The blueshifted South lobe of the original H_2 Cep E outflow is observed at optical wavelengths as Herbig-Haro HH 337, in the shock excited $H\alpha$ and [SII] $\lambda\lambda6717/31$ emission lines (Noriega-Crespo 1997; Devine, Reipurth & Bally 1997). This collisionally excited

emission is characteristic of an extremely low excitation HH object ($\sim 1\%$ ionization) with an anomalously high electron density, $n_e \sim 4100 \text{ cm}^{-3}$, leading to an unusually high pre-shock density of $\sim 10^5 \text{ cm}^{-3}$ (Ayala et al. 2000; hereafter AYA). Both the H α and [SII] emission can be modeled using a J shock of $v_{shock} \sim 15\text{--}30 \text{ km s}^{-1}$ (AYA), although the near-IR H₂ spectra agree better with C-shock models with $v_{shock} \sim 35 \text{ km s}^{-1}$ (Ladd & Hodapp 1997). It has been suggested that a Mach disk produces the optical emission while the IR emission arises from a bow shock (AYA).

Some of the first three dimensional simulations of molecular jets were intended to model the complex structure of the H_2 Cep E outflow (Suttner et al. 1997). Surprisingly they demanded relatively large (> 10^5cm^{-3}) densities, which could be a sign of a very early stage of jet development. This interpretation is consistent with the estimated dynamical age of the Cep E outflow, $\sim 3 \times 10^3$ years (Eislöffel et al. 1996), assuming a distance of 730 pc. The above argument sets a scene in which Cep E is a very young outflow breaking through its placental molecular core.

Our new observations from the *Infrared Space Observatory* (ISO¹) and the *Owens Valley Radio Observatory* (OVRO) millimeter wave array at far/mid infrared and millimetric wavelengths at higher sensitivity and spatial resolution, permit not only a probe of deeper regions of the molecular environment surrounding the outflow, but also a determination of the main excitation and cooling mechanisms. Both are essential to understand the dynamical evolution of very young proto-stellar objects.

In \S 2 and \S 3 we describe the ISO and OVRO observations and data reduction procedures, respectively. The infrared results are presented in \S 4 and further analyzed in \S 5, where we

¹ISO is an ESA project with the instruments funded by ESA Members States (especially the PI countries: France, Germany, the Netherlands and the United Kingdom) and with the participation of ISAS and NASA.

derive the gas physical parameters (such as temperature, density, column density and size of the emitting region) and study the origin of this emission through J and C-shocks and photo-dissociation regions (PDRs). In § 6 we analyze the millimeter results, using the ¹³CO line emission to derive such physical parameters of the outflow as dynamical time scale, mass and mass loss rate, and continuum observations to provide an alternate estimate of the mass of the source. The source spectral energy distribution (SED) is examined in § 7 and in § 8 we summarize our results.

2. ISO Observations and data reduction

The Cep E outflow has been observed with two ISO instruments, the Long Wavelength Spectrometer (LWS, Clegg et al. 1996) and the infrared camera (ISOCAM, Cesarsky et al. 1996). The observations were taken during revolutions 566 (LWS: TDT 56601113 and 56600912) and 792 (CAM: TDT 79200740). The LWS01 grating mode was used to acquire low resolution (R ~ 200) spectra from 43 to 197 μm at two different locations along the flow $(\alpha(2000) = 23\text{h}03\text{m}13.11\text{s}, \delta(2000) = 61^{\circ}42'59.5'')$ for the North lobe and $\alpha(2000) =$ 23h03m12.73s, $\delta(2000) = 61^{\circ}41'56.5''$ for the South lobe). Figure 1 shows the two pointing positions. These spectra are made up of 11 full grating scans oversampled at 1/4 of a resolution element (equivalent to $\sim 0.07~\mu \mathrm{m}$ for $\lambda < 90~\mu \mathrm{m}$ and to $\sim 0.15~\mu \mathrm{m}$ for $\lambda > 90~\mu \mathrm{m}$). The integration time per spectral element was 22 s, corresponding to a total integration time of 1890 s per pointing. The LWS beam is assumed to be $\sim 80''$ in diameter (ISO Handbook, IV, 4.3.2). The ISOCAM (Cesarsky et al. 1996) observations were taken using the Circular Variable Filter (CVF) with a total FOV of $3' \times 3'$, and pixel FOV of 6'' centered on IRAS $23011+6126 \ (\alpha(2000)=23\text{h}03\text{m}13.02\text{s},\ \delta(2000)=61^{\circ}42'26.5'')$. The CVF spectra covered the $5.01-16.77~\mu\mathrm{m}$ wavelength range with a resolving power of $\sim~40$. Each wavelength was observed for ~ 23 sec, for a total on source observing time of 3550 sec.

The LWS Interactive Analysis ² (LIA) Package, Version 7.2 was used to correct the detector dark currents and drifts. Corrected and scan averaged spectra were then analyzed using the ISO Spectral Analysis Package³ (ISAP) Version 2.0. Likewise, the CAM-CVF data were reduced using the Cam Interactive Analysis ⁴ (CIA) standard procedures, and spectra from the individual pixels were extracted using XCVF (Ali 2000), and further analyzed with ISAP.

3. Millimeter observations and data reduction

High resolution millimeter interferometric observations were obtained during 1997 and 2000 using the OVRO millimeter-wave array. The array comprises six 10.4 m antennas that were deployed in three different configurations offering baselines extending from the shadowing limit to 220 m. To ensure the best possible sensitivity to the extended outflow emission, the data from the most compact available configuration is included. Each telescope is equipped with cryogenically cooled SIS receivers providing typical system temperatures of $\sim 300 \text{ K}$ at 110 GHz and $\sim 1200 \text{ K}$ at 222 GHz. Continuum observations employed an analog correlator for total bandwidths of $\sim 2 \text{ GHz}$ and 1 GHz at 222 GHz and 110 GHz (1.3 and 2.7 mm) respectively. The digital correlator was configured to observe simultaneously the 13 CO(1-0) and 18 O(1-0) transitions at 110.2 and 109.8 GHz respectively. For the former isotopomer, spectral resolution was 1.3 km s⁻¹ over a $\sim 80 \text{ km s}^{-1}$ bandwidth, and for the latter, it was 0.3 km s⁻¹ over $\sim 20 \text{ km s}^{-1}$. The half-power beamwidth is $\sim 65''$ at 110 GHz, and $\sim 33''$ at 222 GHz.

²LIA is available at http://www.ipac.caltech.edu/iso/lws/lia/lia.html

³ISAP is available at http://www.ipac.caltech.edu/iso/isap/isap.html

⁴CIA is available at http://www.ipac.caltech.edu/iso/cam/camtools.html

Complex gain calibration was ensured by frequent observations of the quasar BG 0059+58 (= [MFN99] 0059+581). The typical observing cycle alternated scans on Cep E and BG 0059+58 with a period of \sim 20-30 min. 3C 345 and/or 3C 84 were used as passband calibrators while scans on Uranus and/or Neptune were used to set the flux scale. The expected flux calibration uncertainty is \sim 15% at 2.7 mm, and 20-30% at 1.3 mm. Data calibration and editing have been performed using the OVRO-MMA software package (Scoville et al. 1993). Imaging and analysis of the calibrated (u,v) datasets were carried out with the NRAO-AIPS package. All the maps presented in this paper have been obtained with the AIPS IMAGR task using natural weighting of the (u,v) data for the molecular outflow maps and the low spatial resolution continuum maps, while "ROBUST=0" weighting was used for the 1.3 mm high resolution map. The beam sizes and noise levels for the OVRO observations are shown in Table 1.

4. ISO Results

4.1. ISO LWS

Figure 2 shows the LWS far-infrared spectra obtained at the two pointing positions. The strongest features are the atomic fine structure lines of [O I] 63 μ m and [C II] 158 μ m. However, the spectra are also rich in molecular lines from the rotational transitions of CO and H₂O (in both ortho and para form). Two OH lines are also detected in the spectra, but they are too faint to be included in the analysis.

Integrated line fluxes, measured using a gaussian fit, are shown in Table 2, with $1-\sigma$ uncertainties given in parenthesis. In some cases the FWHM was kept fixed to the corresponding instrumental resolution element (i.e. $0.29~\mu m$ and $0.6~\mu m$ for the SW and LW detectors, respectively). This technique was particularly important in the case of faint or/and

blended lines. The uncertainties were obtained either by using ISAP estimated values from the gaussian fit, or by adopting the RMS of the fitted baseline times the resolution element. As expected, both values are very similar.

4.2. ISOCAM CVF

CAM CVF provides spectra covering the 5-17 μ m range over a 32×32 pixel area. Each plane of the cube corresponds to a different λ . Figure 1 shows, as was previously noticed by NCMG, how the morphology at 2 and 7 μ m in the H₂ emission is quite similar. A more detailed description of the CVF emission at each pixel is given in Figure 3. Except at the source position (pixel (16,16)), the 5 to 16 μ m spectra are dominated by the H₂ ground rotational lines from S(7) to S(2). Integrated line fluxes can be found in Table 3. These are corrected for extinction, using an estimated E(B-V) = 1.0 (Lefloch et al. 1996; AYA) and the extinction curve from Draine (1989). The central source is clearly detected and displays strong silicate absorption at 9-12 μ m and CO₂ ice at 15.2 μ m and a number of ice bands (see also Cernicharo et al. 2000). Figure 4 displays the images corresponding to the H₂ 0-0 S(2) to S(7) lines. In accord with expectations based on ground based optical and H₂ observations at 2 μ m, the south lobe is brighter at shorter wavelengths, as the flow breaks through the cloud. The north lobe, buried deeper in the cloud, has fainter S(3) 9.66 μ m and S(2) 12.28 μ m emission, due probably to the broad second maxima at 9.7 μ m due to silicates (Si-O) stretch mode in the extinction curve (Draine 1989, Mathis 1990).

5. Discussion

5.1. The Gas Physical Parameters

5.1.1. CO and H_2O Emission

The CO and H₂O emission can be studied by means of a Large Velocity Gradient (LVG) model in spherical geometry, taking into account the first 35 rotational levels of CO and the first 30 rotational levels of o-H₂O. The collisional rates of Schinke et al. (1985) were used for CO and those of Green, Maluendes and Mc Lean (1993) and Phillips et al. (1996) for H₂O.

There are six main parameters to fit: temperature (T), H_2 density (n(H_2)), CO and o- H_2 O column densities (N(CO) and N(o- H_2 O)), intrinsic width of the line (v_{exp}) and angular size of the emitting area (Ω). To determine all of them simultaneously, two *initial* assumptions are necessary: (1) the CO and o- H_2 O emission arise from the same region; (2) the CO lines are optically thin, i.e. their line fluxes do not depend on their intrinsic widths, while the o- H_2 O lines are optically thick. Since the LWS resolution is too poor to establish size and position of the emitting region, it is difficult to justify (1) from our data. However, in a 15" beam, the H_2 O emission in HH 7-11 appears to arise from the shocked regions already seen in the CO emission bullets (Cernicharo, Gonzalez-Alfonso & Bachiller (1996) and Bachiller & Cernicharo 1990). The adoption of assumption (2) will be confirmed by our models. Figure 5 shows the CO line fluxes as a function of the rotational quantum number, J_{up} , for Cep E North and South lobes. The shape of the distribution is determined only by T and n(H_2), while the absolute fluxes are determined by T, n(H_2) and $\Omega \times N(CO)$, which is proportional to the total number of CO molecules within the emitting volume.

Two extreme cases for each lobe are consistent with the observations. All the models predict that the CO lines are effectively optically thin. Figure 5 shows that the agreement is good for $J_{up}<22$; but for higher J_{up} the models underestimate the observed fluxes. This could indicate the existence of a hotter CO gas component as suggested by Spinoglio et al. (2000) for T Tau.

Assuming that the CO and the o-H₂O line emission is from the same gas, the temperatures

and densities derived from the CO lines can be used to model the o-H₂O line fluxes. Since these lines are optically thick, their absolute fluxes depend on all the free parameters in the model, T, n(H₂), N(o-H₂O), v_{exp} and Ω . Their relative fluxes (or line ratios), on the other hand, do not depend on Ω . Thus, with T and n(H₂) known, the line ratios were modeled and the values of N(o-H₂O) and v_{exp} were constrained. Models of the absolute fluxes then allowed a derivation of Ω . The o-H₂O lines at 179, 174, 113 and 75 μ m were used because they have the highest signal to noise ratio and because the o-H₂O 179 μ m/174 μ m ratio is very sensitive to T and n(H₂).

A summary of the LVG model parameters consistent with the observations can be found in Table 4. A comparison between the LVG models for o-H₂O and the observations is shown in Figure 5. The diameter range estimated for the o-H₂O emitting region is comparable to the extension of the vibrational H₂ 1-0 S(1) 2.12 μm emission, 2700-6900 AU (3.7" - 9.5") at a distance of 730 pc. Knowing the emitting area, we calculate N(CO) and hence the H_2O/H_2 abundance ratio, assuming a standard value of $CO/H_2 \sim 10^{-4}$ in shock regions. For H_2O , an ortho/para ratio of 3 was adopted, leading to predicted p- H_2O fluxes within 3- σ of the observed values. The low temperature models give $H_2O/H_2 \sim 4.0 \times 10^{-5}$ and 1.5×10^{-5} for the North and South lobe respectively. The high temperature models give $H_2O/H_2 \sim 2.5 \times 10^{-4}$ (North) and 2.4×10^{-4} (South). Taking into account these estimates together with their uncertainties, it can be concluded that H₂O abundances are between 100 and 4000 times greater than expected for the ambient medium in cold quiescent conditions, $x(H_2O) \sim 10^{-7}$ (Bergin et al. 1998; Moneti, Cernicharo & Pardo 2000), a result commonly found in young stellar objects (Liseau et al. 1996; Cernicharo et al. 1996; Harwit et al. 1998; Gonzalez-Alfonso et al. 1998; Ceccarelli et al. 1999; Spinoglio et al. 2000). This significant enhancement in the water abundance within outflow regions can be attributed to the vaporization of volatile grain mantles and the increased rate coefficients for specific gas-phase reactions at the elevated gas temperatures reached behind the shocks, and it is expected to persist for $\sim 10^5$ years (Bergin

et al. 1998).

According to the LVG models, the high-J CO emission detected by ISO-LWS indicates a temperature between 220 K and 1200 K. Since the contribution to low-J emission from gas at such temperatures is negligible, the ISO observations must be tracing only the hottest shocked molecular material. By contrast, millimetric observations of the low-J emission (J=2-1, Lefloch et al. 1996 and J=4-3, Hatchell et al. 1999) provide information about the entrained gas.

5.1.2. H_2 Emission

The pure rotational H₂ lines seen in the ISOCAM CVF spectra arise from quadrupole transitions that are always optically thin. Due to their low Einstein coefficients, thermalization is readily possible for moderate volume densities. Hence, LTE calculations are precise enough to compute H₂ column densities. In outflows from YSOs, the H₂ emission is mostly produced by collisional excitation driven by shocks, but to gain some insight into the overall nature of the gas, local thermodynamic equilibrium is commonly assumed. It is then possible to estimate the excitation temperature (T_{ex}) and column density of the H₂ gas using $\ln(N_j/g_j) = \ln(N_{tot})$ /Q) - $E_j/(k T_{ex})$, where $N_j = 4 \pi F_j/(\Omega E_j g_j A_j)$. As usual, A_j is the transition probability (Turner, Kirby-Docken & Dalgarno 1977) and E_i the energy of the upper level (in cgs units) (Dabrowski 1984). The dereddened fluxes, F_j/Ω , are listed in Table 3. The partition function (Q) was calculated assuming an ortho-para ratio of 3. The excitation diagrams, $\ln(N_j/g_j)$ vs E_{up} and the derived excitation temperatures and column densities for several pixels along the flow are shown in Figure 6. Given N_j and T_{ex} , a model spectrum can be created for all H_2 0-0 lines. A comparison one of these models with the observations is shown in Figure 6. A single component model predicts the intensities from the S(3) to the S(7) lines very well, but the intensity of S(2) is systematically underestimated.

5.2. Interpreting the Shock Excited Emission

5.2.1. *C-shocks*

The ground rotational H_2 emission observed in YSOs is mostly attributed to collisional excitation from shocks, either C-type or J-type (Draine & McKee 1993). In a nutshell, C-type shocks are inherently magnetic and less harsh on molecules because Alfvenic waves prepare the gas to the hydrodynamic shock. J-type shocks are mostly hydrodynamic and can dissociate H_2 molecules at lower shock velocities. In the mid and far infrared, where molecular transitions are detected, C-type shocks are expected to be more important. This is confirmed by the comparison of the CO and H_2 pure rotational line fluxes predicted by C-shocks models for $v_{shock} \sim 10-40$ km s⁻¹, and gas densities 10^4-10^6 cm⁻³ (Kaufman & Neufeld 1996), and J-shocks models for $v_{shock} \sim 30-150$ km s⁻¹ and the same gas density range (Hollenbach & McKee 1989). C-shock fluxes are at least 10 times brighter than the J-shocks (and this factor can be much larger depending on the shock conditions). A similar situation is expected for H_2O , and the following analysis assumes that only C-shocks contribute.

The shock velocity and pre-shock density are estimated using the pure rotational H_2 line fluxes and their ratios. From a comparison of these values with C-shock models (Kaufman & Neufeld 1996), we determine a range of $20-40 \text{ km s}^{-1}$ shock velocities, but over a wide range of pre-shock gas densities. The v_{shock} value of $\sim 35 \text{ km s}^{-1}$ derived from the near infrared H_2 emission lines (Ladd & Hodapp 1997), falls within this range. An estimate of the pre-shock gas density can be obtained with the additional assumption that the emission from the pure rotational H_2 and CO lines arise from the same region. If so, the CO/ H_2 cooling ratio can be used in conjunction with the shock velocities. Since this ratio encompasses all cooling, the fraction of lines lying outside the LWS and CVF wavelength coverage must be taken into account. The CO, o- H_2 O and p- H_2 O cooling rates derived from the LVG models can be found in Table 4. For CO, the LVG models neglect the contribution from lines with $J_{up} > 22$,

which may belong to a hotter component. The H_2 cooling was estimated using the simple LTE model and, after taking into account the difference between the LWS and CAM beam, is 1.6×10^{-18} W cm⁻² for both the North and South lobes. Figure 7 shows the comparison between the corrected CO/ H_2 cooling ratios and those predicted by C-type shock models (Kaufman & Neufeld 1996). Within the v_{shock} range of 20–40 km s⁻¹, the models predict a pre-shock density of $10^4 - 2.5 \times 10^5$ cm⁻³.

Figure 8 shows the predicted CO/H₂O cooling ratio as a function of pre-shock density and shock velocity for C-shocks models (Kaufman & Neufeld 1996). The observed (and corrected) ratio for the Cep E outflow indicates shock velocities of 8-14 km s⁻¹, inconsistent with the values derived from the CO/H₂ ratios. This could be due to the fact that the brightest emission regions in H₂ and CO do not seem to coexist spatially, as has been assumed, and therefore trace different gas conditions. Indeed, ¹³CO presented in Figure 9 suggest this may be the case. We discuss this further below. The spatial resolution available with LWS and CAM spectra prevent further discrimination between shock diagnostics.

5.2.2. J-shocks and Photo-Dissociation Regions

The integrated fluxes of the [O I] 63 μ m and [C II] 158 μ m emission are comparable for both the North and South outflows (see Table 2). Since the strength of [C II] line predicted by shock models is several orders of magnitude fainter than the [O I] line, a fraction of the cooling is due to the presence of a PDR or photodissociation region (Hollenbach & Tielens 1999). Most of the [O I] 63 μ m emission is expected to be produced by shock excitation, but a percentage comes from a PDR. And so, to best use the [O I] 63 μ m and [C II] 158 μ m lines as diagnostics of the PDR parameters, an estimate of the [O I] collisional fraction is necessary. For this, we use the additional information provided by the optical forbidden atomic lines (e. g. [O I] λ 6300, [S II] $\lambda\lambda$ 6717/31), and that they are generated by J-shocks, very likely at the Mach

Disk (AYA). Implicitly we are assuming that the molecular emission arises at the bow shock wings, where C-shocks dominate the emission.

Near infrared and optical observations suggest a range of J-type shock velocities of $15-35~\rm km~s^{-1}.~Assuming~v_{shock}=30~\rm km~s^{-1},$ the predicted ratio of [O I] 63 μm to [O I] 6300 Å is $\sim~10~{\rm for~n}=10^5~{\rm cm}^{-3}~$ (Hollenbach & McKee 1989). Since the observed [O I] $\lambda6300$ flux from the south lobe is $4.7 \times 10^{-14} \ \mathrm{erg \ s^{-1} \ cm^{-2} \ arcsec^{-2}}$, the predicted [O I] 63 $\mu \mathrm{m}$ flux over the entire object (r $\sim~2.5$ ") is $9.2 \times 10^{-12}~\rm erg~s^{-1}~cm^{-2}$. This is of order $\sim~25\%$ lower than the LWS flux of $12 \times 10^{-12} \ \mathrm{erg \ s^{-1} \ cm^{-2}}$. From a comparison of J-shock and C-shock models (c.f. Hollenbach & Mckee 1989, Draine, Roberge & Dalgarno 1983; Timmermann 1998), we estimate that at $n = 10^5$ cm⁻³ the contribution of C-shocks to the [O I] 63 μ m flux is about 5-10% that of J-shocks. We will assume that about $\sim~20\%$ of the [O I] 63 $~\mu\mathrm{m}$ flux corresponds to the PDR component. However, the percentage drops as the shock velocity decreases, and indeed for $v_{shock}=20~{\rm km~s^{-1}},$ the collisional emission matches the observed LWS flux. The corrected ratio of [O I] 63 μ m to [C II] 158 μ m emission is then 0.30. With the corrected value of [O I] 63 μ m/[C II] 158 μ m, and the observed LWS [C II] flux of 6.8×10^{-5} erg s⁻¹ cm⁻² sr⁻¹, PDR models can be used to determine the far-ultraviolet (FUV) flux and gas densities required to reproduce the observations. Two of the models of Kaufman et al. (1999) satisfy the above constrains. For one, the incident FUV flux in units of $1.6 \times 10^{-3} {\rm erg \ s^{-1} \ cm^{-2}}$, G_0 , is 30, at a density of 60 cm⁻³, while for the other $G_0 = 6$, at a density of 5500 cm^{-3} .

The integrated flux in the PAHs bands (e.g. at 6.2, 7.7 and 11.3 μ m) is correlated with the FUV radiation field (Boulanger et al. 1998). Thus the existence of a global FUV field can be indirectly inferred from the presence of extended PAHs emission over the entire FOV of the CVF ISOCAM observations (see Figure 3). However, the PAHs emission could arise anywhere along the line of sight to Cep E.

Cep E is near the Cepheus OB3 association (Sargent 1977) with members at distances of 500 - 1000 pc (Crawford & Barnes 1970; Jordi, Trullois & Galadi-Enríquez 1996). Since there are at least 42 bona fide O and B stars in the association (Garmany 1973; Naylor & Fabian 1999), the diffuse FUV field should be sufficient to generate the observed [C II] flux. One member, HD 217086 (O7n), could by itself account for a FUV flux with $G_0 \sim 6$ if it is at 725 pc (Garmany 1973), similar to the distance to Cep E, and separated from Cep E by $\sim 80'$. Hipparcos measurements of HD 217086 give a parallax of 1.20 \pm 0.92 milli-arcsec, approximately 100 pc farther away, but the errors are large.

6. Results from the Millimetric Observations

6.1. ¹³CO Emission

The Cep E outflow can clearly be seen in the 13 CO J = 1-0 transition at 110.2 GHz, shown in Figure 9. One of the most interesting features of this figure is how the 13 CO emission is almost bounded by the H₂ outflow lobes, except at the edge of the south flow, which is breaking through the molecular cloud. Similar behavior is observed for the high velocity CO gas in the HH 211 embedded outflow (Gueth & Guilloteau 1999; Fig 4), and in HH 1/2 (Moro-Martin et al. 1999, Fig 2c).

In LTE approximation, using an excitation temperature of 20 K (Ladd & Hodapp 1997), an abundance of $^{13}\text{CO/H}_2 \sim 1.2 \times 10^{-6}$ and an inclination angle of 45°, the following parameters are derived for the red and blue-shifted outflow lobes respectively: dynamical time scales of 4000 and 8000 years, masses of 0.08 and 0.05 M_{\odot} , kinetic luminosities of 0.1 L_{\odot} for both, and mass loss rates of 7×10^{-6} and 6×10^{-6} $\text{M}_{\odot}/\text{year}$. Nevertheless, these estimates are quite uncertain due to spatial filtering problems, core contamination, and the fact that the edges of the outflow are more than 20 " from the phase center of the map, and thus affected

by primary beam attenuation.

Figure 10 shows a position-velocity diagram along the outflow axis (PA=10°) with the ambient cloud at -11 km s⁻¹ and the outflow extending approximately from 0 to -20 km s⁻¹. Faint $(2-\sigma)$ emission is also seen at ~ 30 and -40 km s⁻¹. We may be tracing high velocity gas that is concentrated nearer to the source than its low velocity counterpart. The left panel of Figure 11 shows the emission from this gas integrated from -47 to -20 km s⁻¹ and from 0 to 25 km s⁻¹. There is no correspondence between this high velocity ¹³CO component and the ¹² CO 4-3 bullets detected by Hatchell, Fuller & Ladd (1999). The latter are $\sim 10''$ away from the core and have velocities of -120 and 60 km s⁻¹ LSR (a velocity range not covered by our observations). A position-velocity diagram along the axis of the second outflow detected in ¹²CO by Ladd & Hodapp (1997) (PA=-45°) was also constructed but no emission was detected.

Images of the $C^{18}O$ J = 1-0 emission at 109.782182 GHz were also made, and show a core surrounded by a poorly imaged halo. There is no evidence of the Cep E outflow, which is not unexpected from this optically thin emission.

6.2. Continuum Emission at 222 GHz and 110 GHz

The right panels of Figure 11 display the continuum emission at 222 GHz and 110 GHz around IRAS 23011+6126. The 222 GHz image shows two unresolved sources in a $1.38''\times1.06''$ beam, with integrated fluxes of 90 mJy and 67 mJy respectively. At 110 GHz, the continuum emission is resolved and has a diameter of $\sim 3''$ or ~ 2200 AU (at 730 pc) and a flux of 35 mJy. It is tempting to interpret this observations as a double source surrounded by an envelope. The presence of a second source strongly suggests that the multiple outflows are due to multiple sources and not to precession. The projected distance between these sources is of $\sim 1.4''$ or ~ 1000 AU at 730 pc. This separation implies a long orbital period, even for an

intermediate mass system, with a range of 7×10^3 - 10^4 yrs, i.e. larger than the kinematical age of the outflow.

Using a dust temperature of 18 K and $\beta \sim 2$ (Ladd and Howe 1997), a gas-to-dust ratio ~ 100 and dust opacities of $0.005~\rm cm^2 g^{-1}$ (Preibisch 1993), the masses associated with the two 222 GHz sources, within 1.4", are 2.5 M $_{\odot}$ and 1.8 M $_{\odot}$. From the 110 GHz continuum, the mass associated with the envelope is found to be 13.6 M $_{\odot}$. Ladd & Howe (1997), for comparison, computed a mass of 10 M $_{\odot}$ within a radius of 3000 AU. At 110 GHz, there is no spatial resolution to separate the two sources.

7. IRAS 23011+6126 Spectral Energy Distribution

The CVF ISOCAM observations clearly detect an embedded source that we identified with IRAS 23011+6126. Figure 12 shows the composite spectral energy distribution (SED) of IRAS 23011+6126. It resembles that of a Class I source (Lada 1987), rather than a Class 0 as proposed by Lefloch et al (1996), based on millimetric observations. Presently, there are reasons to believe that the distinction between Class 0 and Class I is not as sharp as previously thought (see e. g. Gregersen et al. 2000).

Following NCGM, model fits to the SED are calculated assuming: (1) a dust opacity dominated by bare silicates at a temperature of 18 K and a density of $7.5\times10^4 {\rm cm}^{-3}$, and (2) silicates with a thin ice mantle at a temperature of 18 K and a density of $6\times10^4 {\rm cm}^{-3}$. The models assume power-law density and temperature distributions, with a core inner radius of 0.065 AU and outer radius of 2500 AU. As Figure 12 shows, the continuum level of CAM observations near $\log(\nu) \sim 13.3$ is lower than that of the bare silicates model. As the success of the model using silicates with a thin ice mantle suggests, this can be attributed to absorption by ${\rm H_2O}$ at 10-12 $\mu{\rm m}$. The effect has been noticed in other low mass protostars such as Elias 29 (Boogert 1999). This model produces a mass envelope of 13.2 ${\rm M}_{\odot}$ and bolometric luminosity

of $\sim 34~L_{\odot}$. Comparable masses have been obtained assuming a constant density over a spherical volume (10 M_{\odot} , Ladd & Howe 1997) and in dust temperature dependent models (18 M_{\odot} , Lefloch et al. 1996). The bolometric luminosity derived by our models, however, is a factor of 2 smaller that these cases $\sim 30~L_{\odot}$ versus 70 L_{\odot} or 100 L_{\odot} . We suspect the discrepancy is due to the integration methods used, since coarse approximations overestimate the integrated flux. Our estimates of the luminosity and envelope mass are more appropriate for an intermediate mass object rather than a low mass Class I system; although not as massive and luminous as IRAS 05553+1631 (= GAL 192.16-03.82) (Shepherd et al. 1998) or IRAS 20126+4104 (Shepherd et al. 2000).

8. Conclusions

The Cep E outflow has been studied in the mid ($\sim 5-17~\mu m$) and far infrared ($\sim 40-200~\mu m$) using the ISO instruments CAM and LWS, and at millimetric wavelengths (110.2 and 222 GHz) using OVRO. In the near and mid-IR, the Cep E morphology is similar to that expected for a jet driven outflow, where the leading bow shocks entrain and accelerate the surrounding molecular gas (e. g. Raga & Cabrit 1993; Masson & Chernin 1993). As expected, fine structure atomic/ionic emission lines are found, which very likely come from the leading bow shock, in both the Mach Disk and the stagnation tip, where J-shocks are dominant (Figure 13). The H_2 , H_2O and CO molecular emission could arise further 'downstream' at the bow shock wings where the shocks are oblique and more likely to be C-type (Smith 1991). The range of shock velocities to excite these species is $8-35~{\rm km~s^{-1}}$. The ¹³CO emission arises from entrained molecular gas and, as in other outflows, a compact high velocity emission is observed, together with an extended low velocity component that almost coincides spatially with the H_2 near-IR emission. The millimetric continuum emission shows two sources. We identify one of them with IRAS 23011+6126 and we postulate that it is the driver of the

Cep E outflow; the other, also an embedded source, is likely to be driving one of other outflows observed in the region. Finally, the strong [C II] 158 μ m emission must originate from an extended PDR, very likely excited by the nearby Cepheus OB3 association. Our main conclusions are:

- 1. The mid infrared spectra show strong pure rotational H_2 lines, that coincide spatially with the H_2 1-0 S(1) 2.12 μ m emission. Excitation diagrams indicate that this emission is coming from a region at 1000–1300 K, in agreement with the post-shock temperatures expected for shock velocities in the range 20–30 km s⁻¹, consistent with C-shock diagnostics of H_2 line ratios.
- 2. The far infrared spectrum is rich in H_2O and CO lines. The line fluxes can be modeled using an LVG code, assuming that the H_2O and CO emission arises from the same region. Two extreme models fit the observations, with temperatures either of 220 or 1200 K (Table 4). The resulting H_2O abundances are between 100 and 4000 times greater than the one found in quiescent molecular clouds, confirming once more the presence of high water abundance in the shocked gas associated with young stellar outflows. From comparison with shock models, we conclude that C-shocks with $v_{shock} \sim 8-14 \text{ km s}^{-1}$ can reproduce the H_2O and CO observations.
- 3. Two strong atomic lines [O I] 63 μ m and [C II] 158 μ m are present in the LWS spectra. The ratio of their fluxes is close to 1, indicating a PDR origin. Taking into account the significant contribution to the [O I] line from J-shocks, and comparing with PDR models (Kaufman et al 1999), we find that two models reproduce the observations, $G_0 = 30$, n = 60 cm⁻³ and $G_0 = 6$, n = 5500 cm⁻³ erg s⁻¹ cm⁻², where G_0 is the incident FUV flux in units of 1.6×10^{-3} erg s⁻¹ cm⁻². Cep E is relatively close to the Cepheus OB3 association, which can produce the diffuse FUV field required by these models.
- 4. The bipolar outflow can be seen in the high resolution 13 CO image at 110.2 GHz. This emission is bounded by the H_2 condensations. Outflow velocities extend from 0 to -20 km s⁻¹,

and are centered on the ambient cloud velocity of -11 km s⁻¹. There is also evidence for high velocity gas at 30 and -40 km s⁻¹ very close to the source. From the ¹³CO observations we estimate, for the North and South outflows lobes respectively, time scales of 4000 and 8000 years, masses of 0.08 and 0.05 M_{\odot} , similar kinetic luminosities of $0.1L_{\odot}$ for both, and mass loss rates of 7×10^{-6} and 6×10^{-6} L_{\odot}/year . This confirms that the outflow is very young as the high water abundance seems to indicate.

- 5. The continuum images at 222 GHz show the presence of two unresolved sources within the positional error bars of IRAS 23011+6126. The masses associated with them are 2.5 ${\rm M}_{\odot}$ and 1.8 ${\rm M}_{\odot}$. The lower spatial resolution of the continuum observations at 110 GHz allow us to detect the surrounding envelope which has a mass of 13.6 ${\rm M}_{\odot}$ and a radius of 1100 AU. No evidence is found for any of the other outflows observed at near-infrared of radio wavelengths. The presence of a second source, however, strongly suggests that the multiple outflows are due to multiple sources and not to precession. The separation of these sources is about 1.4"or \sim 1000 AU, and so even for an intermediate mass system, the binary period would be of the order of $7 \times 10^3 10^4$ yrs, which is longer than the kinematical age of the outflow.
- 6. A simple envelope model for the spectral energy distribution of IRAS 23011+6126 predicts a mass envelope of 13.2 M_{\odot} and a luminosity of $\sim 30 L_{\odot}$ from silicates with thin ice mantles. The spectral features observed at 5–17 μ m in IRAS 23011+6126 are closer to those of a Class I source, and the mass and luminosity estimated are those of an intermediate mass YSO, rather than a low mass Class 0 object.

We thank Babar Ali of the IPAC ISO group for his insights on the ISOCAM data reduction, and John Bieging and the referee for their helpful comments. A.N-C. & S.M. work was supported in part by JPL, California Institute of Technology, under a contract with NASA. L.T. was partially supported by the Agenzia Spaziale Italiana through grant ASI

ARS-78-1999. J. Cernicharo thanks Spanish DGES for support under grants PB96-0883 and PNIE98-1351. The ISO Spectral Analysis Package (ISAP) is a joint development by the LWS and SWS Instrument Teams and Data Centers. Contributing institutes are Centre d'Etude Spatiale des Rayonnements (France), Institute d'Astrophysique Spatiale (France), Infrared Processing and Analysis Center (United States), Max-Planck-Insitut für Extraterrestrische Physisk (Germany), Rutherford Appleton Laboratories United Kingdom) and the Space Research Organization, Netherlands. The Owens Valley millimeter-wave array is supported by NSF grant AST-99-81546. Research on young star and disk systems is also supported by the Norris Planetary Origins Project and NASA's Origins of Solar Systems program (through grant NAG-5-4591).

REFERENCES

Ali, B. 2000 (private communication)

Ayala, S., Noriega-Crespo, A., Garnavich, P., Curiel, S., Raga, A.C., & Böhm K.H. 2000, AJ, 120, 909

Bergin, E.A., Melnick, G.J., & Neufeld, D.A. 1998, ApJ 499, 777

Boogert, A.C.A. 1999 PhD Thesis, University of Groningen

Boulanger, F., Abergel, A., Bernard, J.P., et al. 1998, in ASP Conf. Proc. 132, "Star Formation with the *Infrared Space Observatory*", ed. J. Yun & R. Liseau (San Francisco: ASP), 15

Ceccarelli, C., Caux, E., White, G.J., et al. 1998, A&A, 331, L17

Ceccarelli, C., Caux, E., Loinard, L. et al. 1999, A&A, 342, L21

Cesarsky, C., Abergel, A., Agnese, P., et al. 1996, A&A, 315, L32

Bachiller, R., & Cernicharo, J. 1990, A&A, 236, 276

Cernicharo, J., Gonzalez-Alfonso, E., & Bachiller, R., 1996, A&A, 305, L5

Cernicharo, J., Noriega-Crespo, A., Cesarsky, D., et al. 2000, Science, 288, 649

Cesarsky, D., Cox, P., Pineau Des Forêts, G., van Dishoeck, E.F., Boulanger, F. & Wright C. M. 1999, A&A, 348, 945

Clegg, P.E., Ade, P.A.R., Armand, C., et al. 1996, A&A, 331, 372

Crawford, D.L. & Barnes, J.V. 1970, AJ 75, 952

Devine, D., Reipurth B., & Bally J. 1997 in "Low Mass Star Formation from Infall to Outflow" Ed. F. Malbet & A. Castets, p91 Draine, B.T. et al. 1983

Draine, B.T. 1989, in Proc. 22nd ESLAB Symp. on IR Spectroscopy in Astronomy, ed. B.H. Kaldeich, ESA SP-290, 93

Draine, B.T., & McKee, C.F. 1993, ARA&A, 31, 373

Dabrowski, I. 1984, CanJPhys, 62, 1639

Eislöffel, J., Smith, M.D., Davis, C.J., & Ray, T.P. 1996, AJ, 112, 2086

Fukui, Y. 1989, in "Low Mass Star Formation and Pre-Main Sequence Objects", ESO 1989, ed. B. Reipurth, p95.

Garmany, C.D. 1973, AJ, 78, 185

Gonzalez-Alfonso, E., Cernicharo, J., van Dishoeck, E., Wright, C.M., & Heras, A. 1998, ApJ 502, L169

Green, S., Maluendes, S., & McLean, A.D. 1993, ApJS, 85, 181

Gregersen, E.M., Evans, N.J., Maradones, D., & Myers, P.C. 2000, ApJ, 533, 440

Gueth, F., & Guilloteau, S. 1999, A&A, 343, 571

Hartigan, P., Raymond, J., & Hartmann, L. 1987, ApJ, 316, 323

Harwit, M., Neufeld, D.A., Melnick, G.J., & Kaufman, M.J. 1998, ApJ, 497, L105

Hatchell, J., Fuller, G.A., & Ladd, E.F. 1999, A&A, 346, 278

Hildebrand, R. H. 1983, QJRAS, 24, 267

Hodapp, K.-W. 1994, ApJS, 94, 615

Hollenbach, D., & McKee, C.F. 1989, ApJ, 342, 306

Hollenbach, D.J., & Tielens, A.G.G.M. 1999, RvMP, 71, 173

ISO Handbook, http://www.iso.vilspa.esa.es/users/handbook/

Jordi, C., Trullois, E. & Galadi-Enríquez, D. 1996, A&A, 312, 499

Kaufman M.J., & Neufeld, D.A. 1996, ApJ, 456, 250

Kaufman, M.J., Wolfire, M.G., Hollenbach, D.J., & Luhman, M.L. 1999, ApJ, 527, 795

Lada, C.J. 1987, IAU Symposium 115, "Star Forming Regions", p1

Ladd, E.F., & Hodapp, K. 1997, ApJ, 474, 749

Ladd, E.F., & Howe, J.E. 1997 in "Low Mass Star Formation from Infall to Outflow" Ed. F. Malbet & A. Castets, p145

Lefloch, B., Eislöffel, J., & Lazareff, B. 1996, A&A, 313, L17

Liseau, R., Ceccarelli, C., Larsson, B., et al. 1996, A&A, 315, L181

Masson, C.R., & Chernin, L.M. 1993, ApJ, 414, 230

Mathis, J.S. 1990, ARAA, 28, 37

Molinari, S., Ceccarelli, C., White, G.J., et al. 1999, ApJ, 521, L71

Molinari, S., Noriega-Crespo, A., Ceccarelli, C., et al. 2000, ApJ, 538, 698

Moneti, A., Cernicharo, J., & Pardo, J.M. 2000, submitted

Moro-Martín, A., Cernicharo, J., Noriega-Crespo, A., & Martín-Pintado 1999, ApJ, 520, L111

Naylor, T. & Fabian A.C. 1999, MNRAS 302, 714

Noriega-Crespo, A. 1997, in "Herbig-Haro Flows and the Birth of Low Mass Stars" Ed. B. Reipurth & C. Bertout, p103.

Noriega-Crespo, A, Garnavich, P.M. & Molinari, S. 1998, AJ, 116, 1388

Phillips, T.R., Maluendes, S., & Green, S. 1996, ApJS, 107, 467

Preibisch, Th., Ossenkopf, V., Yorke, H.W., & Henning, Th. 1993, A& A, 279, 577

Raga, A., & Cabrit, S. 1993, A&A, 278, 267

Reipurth, B., & Raga, A.C. 1999 in "The Origin of Stars and Planetary Systems", ed Ch. Lada & D. Kylafis, p267

Sargent, A. 1997, ApJ, 218, 736

Schinke, R., Engel, V., Buck, U., Meyer, H., & Diercksen, G.H.F. 1985, ApJ, 299, 939S

Scoville N.Z., Carlstrom J.E., Chandler C.J., et al. 1993, PASP, 105, 1482

Shepherd, D.S., Watson, A.M., Sargent, A.I., & Churchwell, E. 1998, ApJ, 507, 861

Shepherd, D.S., Yu, K.C., Bally, J., & Testi, L. 2000, ApJ, 535, 833

Smith, M.D., 1991, MNRAS, 253, 175

Spinoglio, L., Giannini, T., Nisini, B., et al. 2000, A&A, 353, 1055

Suttner, G., Smith, M.D., Yorke, H.W., & Zinnecker, H. 1997, A&A, 318, 595

Timmermann, R. 1998, ApJ, 498, 246

Turner, J., Kirby-Docken, K., & Dalgarno, A. 1977, ApJS, 35, 281

van den Ancker, M.E. 1999, PhD Thesis, University of Amsterdam

This manuscript was prepared with the AAS LATEX macros v4.0.

Table 1. OVRO observations

Map	Beam Size(") (PA°)	RMS noise $(1-\sigma)$
110 GHz (cont.)	3.1×2.8 (-86°)	1 mJy/beam
222 GHz (cont.)	1.4×1.0 (-78°)	7 mJy/beam
$C^{18}O$ (1-0)	$8 \times 7 \ (+63^{\circ})$	0.05 Jy/beam/channel
$^{13}CO (1-0)$	$8 \times 7 \ (+54^{\circ})$	0.03 Jy/beam/channel

Table 2. Cep E LWS Integrated Fluxes $^{\rm a}$

$\lambda(\mu \mathrm{m})$	Element	Transition	North	South	
63.18	[O I]	$3P_1-3P_2$	9.3(0.5)	12.1(0.7)	
75.38	$\text{o-H}_2\text{O}$	3_{21} - 2_{12}	1.8(0.4)	$0.9(0.2)^{b}$	
78.74	$\text{o-H}_2\text{O}$	4_{23} - 3_{12}	$0.6(0.5)^{b}$		
79.36	CO	33-32	$1.3(0.4)^{b}$		
82.03	$\text{o-H}_2\text{O}$	6_{16} - 5_{5}		$0.9(0.4)^{b}$	
84.60	ОН	3/2-3/2 (7/2-5/2+4-3)	$1.5(0.4)^{b}$	$0.8(0.3)^{b}$	
89.99	$\mathrm{p\text{-}H}_2\mathrm{O}$	3_{22} - 2_{11}		$1.0(0.2)^{c}$	
96.77	CO	27-26	1.2(0.2)	0.8(0.1)	
99.49	$\text{o-H}_2\text{O}$	5_{5} - 4_{14}	$1.2(0.4)^{d}$	$0.7(0.3)^{d}$	
100.46	CO	26-25	$0.6(0.4)^{d}$	$0.8(0.6)^{d}$	
100.91	$\text{o-H}_2\text{O}$	5_{14} - 4_{23}	$1.0(0.4)^{d}$		
104.44	CO	25-24	0.7(0.3)		
108.07	$o-H_2O$	2_{21} - 1_{10}	$2.6(0.5)^{d}$	$0.9(0.4)^{d}$	
108.76	CO	24-23	1.0(0.8)	1.1(0.6)	
113.54	$\text{o-H}_2\text{O}$	4_{14} - 3_{3}	$2.7(0.3)^{f}$	$1.6(0.3)^{d,f}$	
119.44	ОН	3/2-3/2 (5/2+-3/2- 2-1)	0.3(0.1)	0.5(0.1)	
125.35	$\mathrm{p\text{-}H}_2\mathrm{O}$	4_4 - 3_{13}	0.3(0.1)	0.4(0.2)	
126.71	$\mathrm{p\text{-}H}_2\mathrm{O}$	3_{31} - 3_{22}	0.4(0.2)	0.3(0.2)	
130.37	CO	20-19	0.7(0.1)	$0.8(0.1)^{d}$	
137.20	CO	19-18	0.7(0.1)	$1.0(0.2)^{d}$	
138.53	$\mathrm{p\text{-}H}_{2}\mathrm{O}$	3_{13} - 2_2	0.3(0.1)	$0.5(0.2)^{d}$	
144.78	CO	18-17	$1.2(0.2)^{d}$	$1.4(0.4)^{d}$	
145.52	[O I]	$3P_0-3P_1$	$< 0.3^{d}$	$0.9(0.6)^{d}$	
153.27	CO	17-16	1.0(0.1)	$1.9(0.1)^{d}$	

Table 2—Continued

$\lambda(\mu \mathrm{m})$	Element	Transition	North	South
15774	[C II]	on on	7 0/0 2)d	0.1/0.0)d
157.74	[C II]	$2P_{3/2}$ - $2P_{1/2}$	$7.0(0.3)^{\alpha}$	$8.1(0.2)^{d}$
162.81	CO	16-15	1.7(0.1)	$1.9(0.1)^{d}$
173.63	CO	15-14	$2.1(0.6)^{d}$	$2.2(0.6)^{d}$
174.62	$o-H_2O$	3_3 - 2_{12}	$1.6(0.9)^{d}$	$1.5(1.0)^{d}$
179.53	$o-H_2O$	2_{12} - 1_1	$2.7(0.2)^{d}$	$3.1(0.4)^{d}$
185.99	CO	14-13	2.1(0.2)	$2.3(0.2)^{d}$

 $^{^{\}rm a}{\rm In}$ units of $10^{-19}{\rm W/cm^2}.~1\mbox{-}\sigma$ uncertainties are given in parenthesis.

Horizontal dotted lines indicate non detections

 $^{^{\}rm b}{\rm FWHM}$ was fixed at 0.29 $\mu{\rm m}.$

 $^{^{\}rm c} Blended$ with CO 29-28 90.16 $\mu m.$

 $^{^{\}rm d}{\rm FWHM}$ was fixed at $0.60\mu{\rm m}.$

 $^{^{\}mathrm{e}}\mathrm{Blended}$ with p-H₂O $2_{20}\text{-}1_{11}$ 100.98 $\mu\mathrm{m}.$

 $^{^{\}rm f} Blended$ with CO 23-22 113.76 $\mu m.$

Table 3. Rotational H_2 0-0 Observed Fluxes^a

$\operatorname{Line}(\mu\mathrm{m})$	(15,12)	(15,13)	(15,14)	(17,17)	(17,18)	(17,19)	(19,21)
S(7) 5.51	3.9(0.6)	4.3(0.5)	2.0(0.3)	2.3(0.3)	7.5(0.5)	4.1(0.2)	1.5(0.3)
S(6) 6.11	3.1(0.5)	3.3(0.4)	1.0(0.2)	0.9(0.2)	4.1(0.2)	2.2(0.3)	1.5(0.3)
S(5) 6.91	5.7(0.2)	7.2(0.3)	3.8(0.2)	5.1(0.3)	12.7(0.6)	6.5(0.3)	3.3(0.1)
S(4) 8.02	3.5(0.2)	4.2(0.2)	2.0(0.2)	1.4(0.2)	2.6(0.2)	1.8(0.1)	1.6(0.1)
S(3) 9.66	2.5(0.2)	4.3(0.2)	3.2(0.1)	1.9(0.1)	5.2(0.3)	3.8(0.2)	1.9(0.1)
S(2) 12.28	2.0(0.2)	4.0(0.3)	3.1(0.2)	1.4(0.1)	1.9(0.2)	1.6(0.2)	1.3(0.2)

 $^{^{\}rm a}{\rm Fluxes}$ dereddened by E(B-V) = 1.0, in units of $10^{-11}~{\rm W/cm^2/sr}$

Table 4. LVG parameters

	Nor	th	South		
	220	1.200	24 5	1200	
Temperature (K)	220	1200	215	1200	
$n(H_2) (10^6 cm^{-3})$	2.0	0.02	4.0	0.04	
$v_{exp} (km s^{-1})$	20-40	25-40	30-40	15-60	
Source Diameter (")	5.1-3.7	5.7-4.3	5.8-5.1	9.5 - 4.7	
$N_{CO} (10^{17} cm^{-2})$	9.5-18.0	16-26	7.3-9.3	2.8-11.3	
$N_{o-H2O} (10^{17} cm^{-2})$	3-5	30-50	0.8-1.0	5-20	
$N_{p-H2O} (10^{17} cm^{-2})$	1-1.7	10-16.7	0.27-0.3	1.7-6.7	
$L_{CO} (10^{-18} \text{ W cm}^{-2})^{\text{a}}$	2.1	2.6	2.4	2.8	
$L_{o-H2O} (10^{-18} \text{ W cm}^{-2})^{\text{b}}$	1.8	2.1	1.3	2.1	
$L_{p-H2O} (10^{-18} \text{ W cm}^{-2})^{c}$	0.6	0.6	0.4	0.6	

 $^{^{\}rm a}{\rm Observed}$ CO fluxes are 14.3(1.2) × 10^{-19} (North) and 14.2(1.2) × 10^{-19} W cm $^{-2}$ (South)

 $[^]b Observed~o\text{-H}_20$ fluxes are $14.2(1.4)\times~10^{-19}$ (North) and $9.6(1.3)\times~10^{-19}~\rm W~cm^{-2}$ (South)

 $^{^{\}rm c} \rm Observed~p\text{-}H_20~fluxes~are~1(0.3)\times~10^{-19}~(North)~and~2.2(0.4)\times~10^{-19}~W~cm^{-2}~(South)$

Figure Captions

- Fig. 1.— ISOCAM-CVF observations of the Cep E outflow at H₂ 0-0 S(5) 6.1 μ m. The grey scale depicts the H₂ 0-0 S(5) 6.91 μ m continuum-subtracted emission, and the superimposed contour image is the NIR vibrational H₂ 1-0 S(1) 2.121 μ m line (AYA). The FOV is $\sim 2'$. The locations of the LWS circular apertures are also shown in the image (r $\sim 40''$), where the crosses represent the two pointing positions.
- Fig. 2.— ISO-LWS spectra of the Cep E North and South lobes after continuum subtraction and averaging over all detectors. Integrated line fluxes are given in Table 2.
- Fig. 3.— ISOCAM-CVF observations of Cep E outflow. In grey scale is the H_2 0-0 S(5) 6.91 μ m image. Superimposed are the background subtracted spectra obtained at several positions along the outflow. Their scale is identical to that of the two magnified spectra shown in the upper left, for one position in the South and one in the North lobe. The spectrum at the central source position, IRAS 23011+6126, is shown in the lower right on a different scale. Below it, is the spectrum of the background averaged over 100 pixels. Orientation and pixel size are indicated in the figure.
- Fig. 4.— ISOCAM CVF images of the Cep E outflow at the rotational H_2 0-0 lines, after the emission from the adjent line-free planes have been subtracted. All contour levels are from 0.3 to 3.1 by 0.4, in units of 10^{-9} W/cm²/sr. The figures have been plotted in different grey scales to enhance the contrast. The crosses indicate the position of the source.
- Fig. 5.— Comparison between the LVG predictions and the observations for CO and H₂O lines fluxes. (a) CO line fluxes versus the rotational quantum number J_{up} for Cep E North lobe. Error bars indicate 1- σ uncertainties. The two extreme LVG models that fits the observations are shown in solid (T = 220 K, n(H₂) = 2×10⁶ cm⁻³, N(CO) = 8.65×10¹⁷ cm⁻², D = 5.1", $v_{exp} = 20 \text{km s}^{-1}$) and dashed (T = 1200 K, n(H₂) = 2×10⁴ cm⁻³, N(CO) = 1.6×10¹⁸ cm⁻², D

= 5.7", $v_{exp} = 25 \text{ km s}^{-1}$) lines. (b) Same as (a) for Cep E South lobe. The two LVG models are in solid (T = 215 K, n(H₂) = $4 \times 10^6 \text{ cm}^{-3}$, N(CO) = $7.3 \times 10^{17} \text{ cm}^{-2}$, D = 5.8", $v_{exp} = 30 \text{ km s}^{-1}$) and dashed (T = 1200 K, n(H₂) = $4 \times 10^4 \text{ cm}^{-3}$, N(CO) = $1.1 \times 10^{17} \text{ cm}^{-2}$, D = 15", $v_{exp} = 50 \text{ km s}^{-1}$) lines. (c) Ratio between LWS fluxes of o-H₂O lines and LVG model predictions for Cep E North lobe. Error bars represent 1- σ uncertainties. Open squares correspond to the low temperature LVG model (same parameters as above with N(o-H₂O) = $3 \times 10^{17} \text{ cm}^{-2}$), while crosses correspond to the high temperature model (with N(o-H₂O) = $3 \times 10^{18} \text{ cm}^{-2}$). (d) Same as (c) for Cep E South lobe. Open squares correspond to the low temperature LVG model (with N(o-H₂O) = $8 \times 10^{16} \text{ cm}^{-2}$), while crosses correspond to the high temperature model (with N(o-H₂O) = $1 \times 10^{17} \text{ cm}^{-2}$)

Fig. 6.— Determination of the H_2 temperature and column density from the H_2 0-0 rotational lines observed with ISOCAM-CVF (corrected by extinction, E(B-V)=1.0). The first panel is the dereddened observed spectra(solid line) at pixel (15,12), together with the model (dotted line) derived from the fitted temperature and column densities. On the right is the excitation diagram and the best-fit parameters for this pixel. The rest of the panels show the excitation diagrams for six positions along the flow with their corresponding best-fit values.

Fig. 7.— CO/H₂ (rotational) cooling ratio (grey scale) as a function of pre-shock density and shock velocity for C-shocks models (with B = $(n_H/cm^{-3})^{1/2} \mu$ G; from Kaufman and Neufeld 1996). The coolings obtained from the 200 K and 1200 K LVG models for Cep E North and South lobes are shown in dashed and dotted lines respectively. Contour levels are from 0 to 6.4 by 0.4.

Fig. 8.— CO/H₂O cooling ratio (grey scale) as a function of pre-shock density and shock velocity for C-shocks models (with B = $(n_H/cm^{-3})^{1/2} \mu$ G; from Kaufman and Neufeld 1996). The coolings obtained from the 200 K and 1200 K LVG models for Cep E North and South lobes are shown in dashed and dotted lines respectively. Contour levels are from -1 to 2.25 by

0.25.

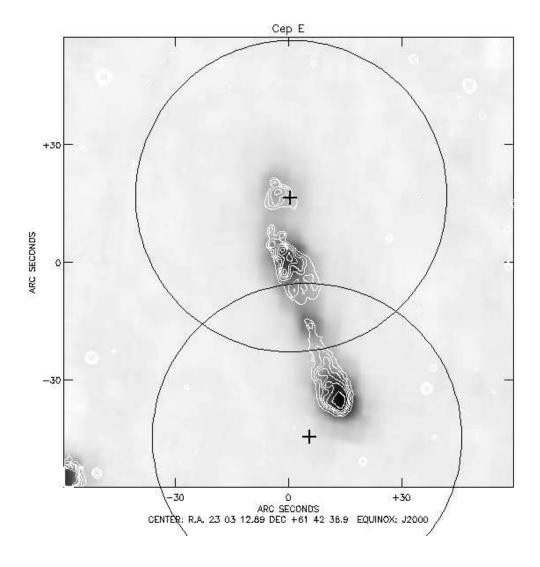
Fig. 9.— Superposition of the H₂ 1-0 S(1) 2.12 μ m emission (in grey scale) on the ¹³CO and 222 GHz continuum in contours. The dashed contours towards the north correspond to the red-shifted lobe (v_{LSR} = -9.5 to -2.5 km s⁻¹), while the solid contours to the south correspond to the blue-shifted lobe (v_{LSR} = -20.5 to -13.5 km s⁻¹). Contour levels for ¹³CO are 0.4 to 3.0 by 0.4 and 0.2 to 1.4 by 0.2 respectively (in Jy/beam). Contour levels for 222 GHz are from 0.02 to 0.05 by 0.01 (in Jy/beam). The beam size is showed at the lower right corner.

Fig. 10.— Position velocity diagram in the 13 CO J=1-0 transition along the axis of the Cep E outflow. The lowest contour correspond to a 2- σ level.

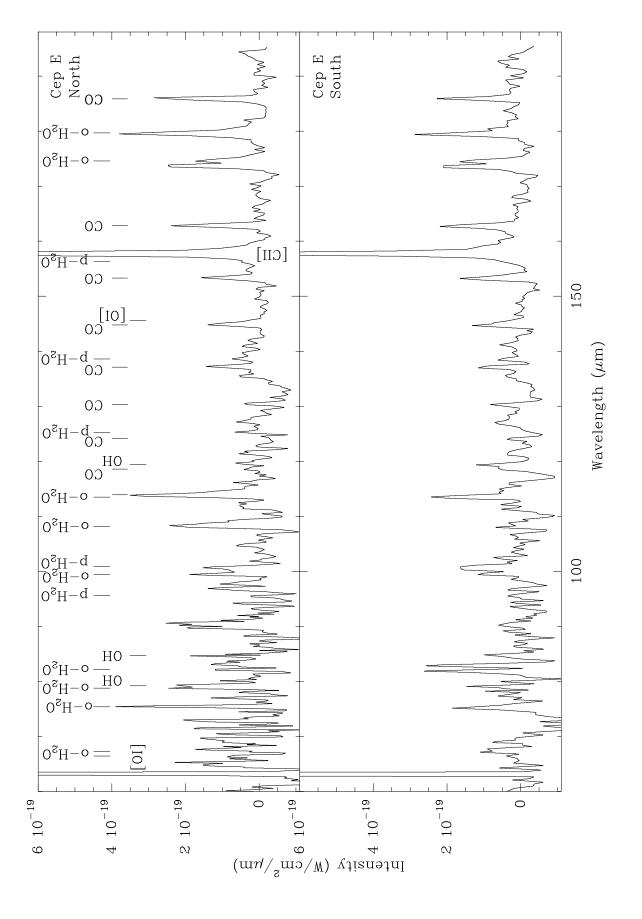
Fig. 11.— Left: same as Figure 9 but for the high velocity gas. The red lobe corresponds to the gas with velocities between 0 and 20 km s⁻¹ (dotted contours) and the blue lobe to gas with velocities between -47 and -20 km s⁻¹(solid contours). The contour levels are 10 and 15 in both cases. The detections are at 5-7 σ level. Right: 222 GHz and 110 GHz continuum image centered on IRAS 23011+6126. The flux levels are from 0.02 to 0.05 by 0.01 and from 0.003 to 0.02 by 0.003 respectively (in Jy/beam).

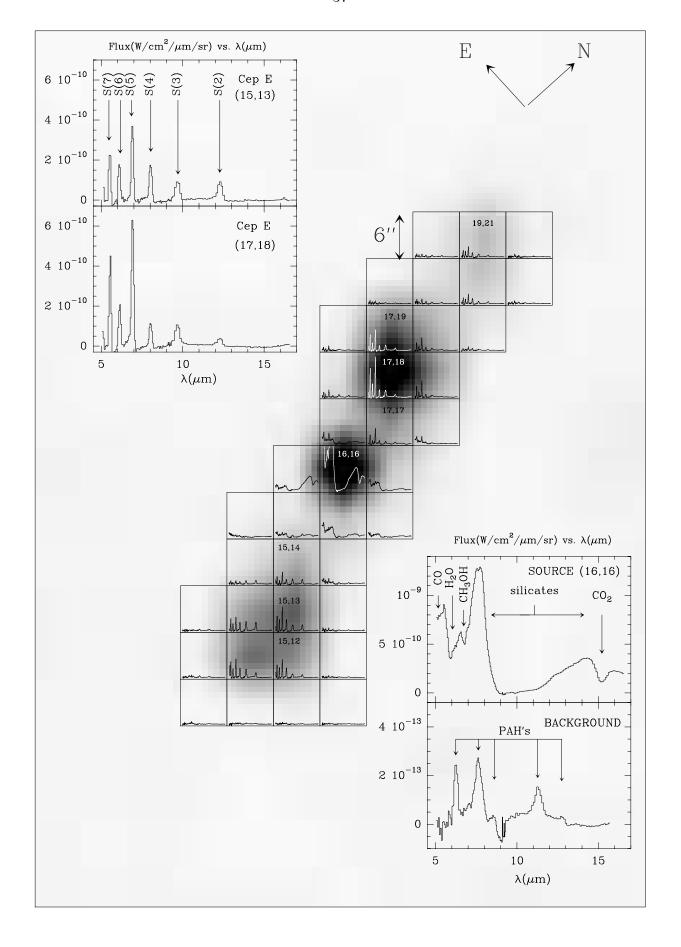
Fig. 12.— Spectral energy distribution of IRAS 23011+6126. Data points are taken from Ladd & Howe 1997 (submillimeter; squares), from Noriega-Crespo et al. 1998 (IRAS and ISOCAM; open triangles and upper limit) and from our new OVRO results (filled symbols). The thick solid line represents the CVF spectra extracted at the source position. A model assuming a dust opacity dominated by bare silicates, at a temperature of 18 K and $n = 7.5 \times 10^4 \text{cm}^{-3}$ is shown in solid line. The dotted line is for silicates with a thin ice mantle at the 18 K and $n = 6 \times 10^4 \text{cm}^{-3}$.

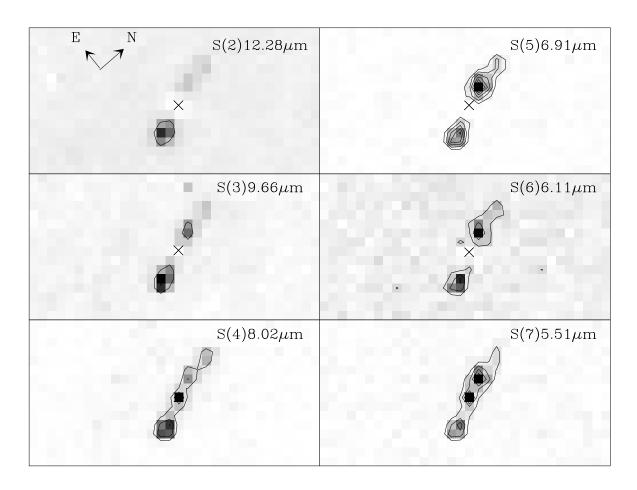
Fig. 13.— Schematic view of the different emitting regions in the Cep E outflow adopting a iet-driven model.

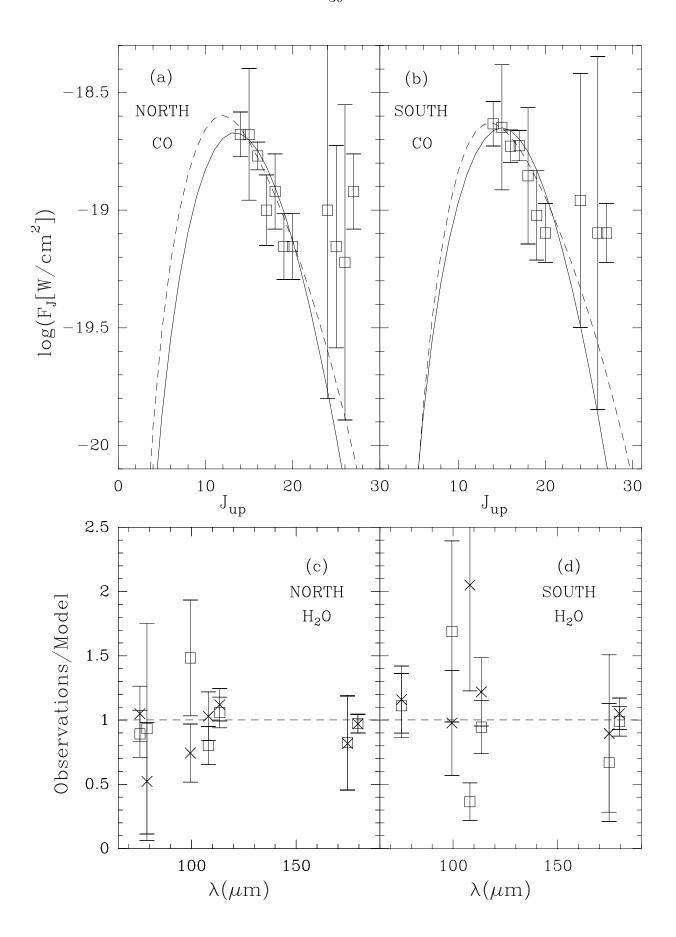


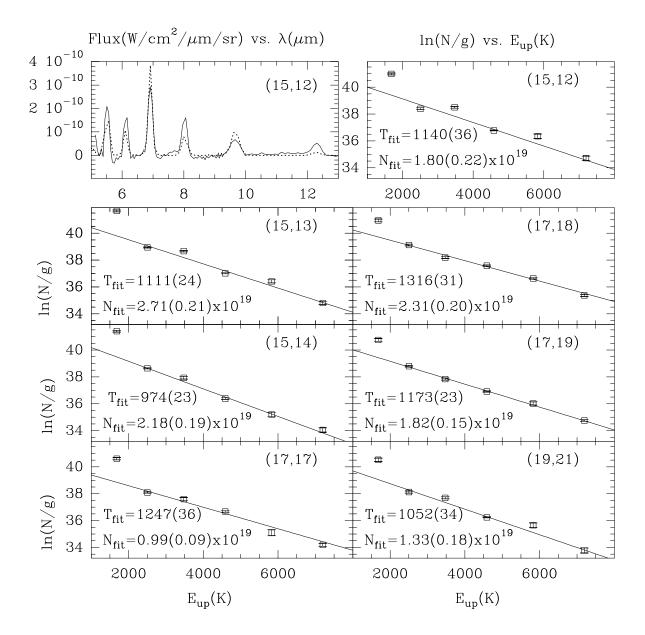


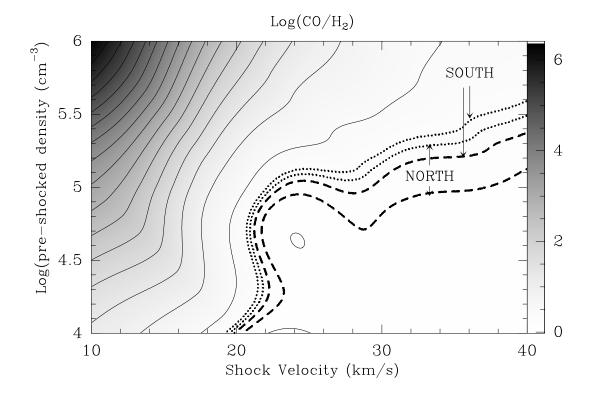


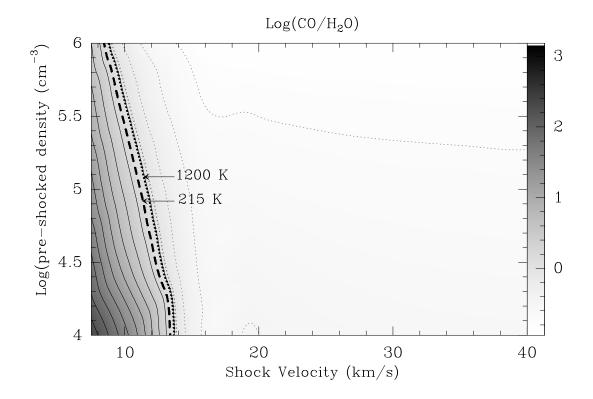


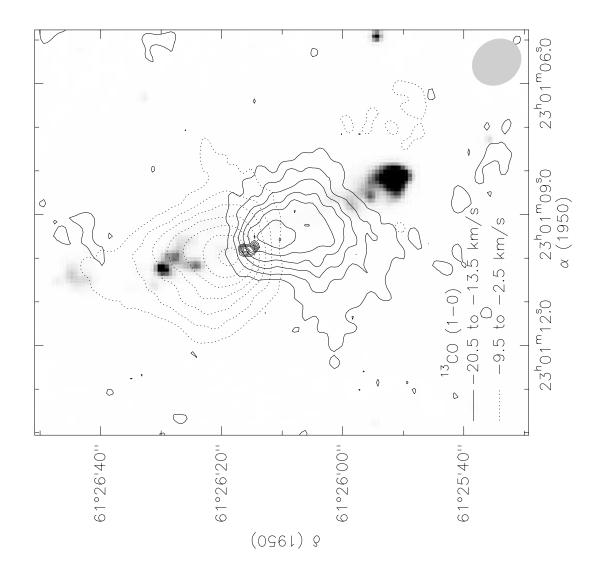


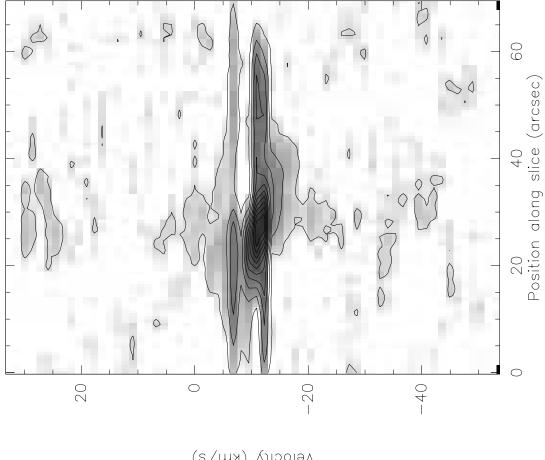












Velocity (km/s)

